

Acknowledgements

I would like to express my deepest appreciation to my thesis adviser, Dr. Kwong Lau, who during these years demonstrated how to think and act as a physicist. I learned to develop a sense of numbers and to do orders of magnitude estimation before any careful calculation. This way I gain deeper physics insights without getting lost in complicated equations and numerous numbers. Moreover, he taught me the attitudes a physicist should hold. First, always doubt. It is not only because in the history of science many breakthroughs were brought about by careful inspection of previous works, but because only after I manage to verify the previous works do I gain deeper understanding. Second, be bold. Do not hesitate to show something new even if it is not fully understood. After all, there is no perfect analysis; *JL* One can always improve it. In addition, I have to thank him for sending me to Daya Bay onsite, where I participated in many Daya Bay installation activities and gained precious experience in the construction of a large physics project.

I would like to thank my committee members for the insightful opinions on my work. Dr. Bellwied's advanced particle physics class sharpens and broadens my knowledge in particle physics. Dr. Hungerford's valuable inputs on my neutron study introduced me to the Monte Carlo studies on this difficult topic. Dr. Pinsky, who is also my Daya Bay colleague, had enlightening conversation with me about physics in general.

I have to express thanks to my Daya Bay colleagues, Dr. Kam-Biu Luk and Dr. Randy Johnson, with whom I worked at Daya Bay and gained valuable hardware experience in

Abstract

The Daya Bay Reactor Neutrino Experiment is designed to measure the neutrino mixing angle, θ_{13} , with a sensitivity of $\sin^2 2\theta_{13} < 0.01$ at 90% confidence level. Neutrons produced by cosmic muon spallation constitute one of the main backgrounds, and an understanding of the neutron yield of a muon is important. Since Daya Bay has a very good muon tracking system, muon tracks can be reconstructed accurately. The neutron yield can be determined by constructing a fiducial volume around each muon track. The neutron yield is found to be of the order of $10^{-4} \text{ cm}^2/\mu/\text{g}$ for each experimental hall of Daya Bay. The results show a gradual dependence on muon energy, and are in agreement with other measurements. Since Daya Bay is capable of measuring energy deposition, the neutron events show enhanced energy deposition.

any more results?
If so - add to abstract

Run on
Sentences.

the strangeness content of \bar{K}^0 is different from that of K^0 , the phenomenon is called strangeness oscillation. Although K^0 and \bar{K}^0 are produced via the strong force, they decay weakly. There are two weak eigenstates K_L and K_S corresponding to very different lifetime with subscripts meaning long and short, respectively, and the strong eigenstates can be written as linear combinations of the weak eigenstates. The oscillation is caused by the slight difference in their masses and by measuring the appearance probability of \bar{K}^0 in the K^0 as a function of time, one can obtain the mass splitting of K_L and K_S [3] [4].

In the late 1960s the Homestake Experiment directed by R. Davis measured the neutrino flux from the Sun and found the flux was only about one-third of the prediction from the Standard Solar Model [5]. This discrepancy is known as the Solar Neutrino Problem. In 1962, the muon neutrino was discovered [6], signaling the existence of more than one species of neutrino. In 1969, as an attempt to solve the solar neutrino problem, a theory of massive neutrinos [7] was proposed in which neutrinos oscillate between 2 different flavors as they propagate in space. The existence of the third kind of neutrino, ν_τ was immediately postulated when a third lepton, the τ , was discovered in 1975, and the discovery of ν_τ had to wait until July 2000 [8].

The first definitive evidence of neutrino oscillation came in 1998. Super-Kamiokande published its observation [9] that fewer ν_μ come from the bottom of the detector than from the top by measuring the muons produced by charge current interactions which is consistent with the $\nu_\mu \leftrightarrow \nu_\tau$ oscillation hypothesis because neutrinos from the bottom of the detector have to travel through the earth to reach the detector. In 2001 the Sudbury Neutrino Observatory (SNO) in Canada confirmed the solar neutrino oscillation. The weak interaction is mediated by the exchange of weak bosons. Interactions involving the exchange of charged bosons are called charged current interactions, while those involving the exchange of neutral bosons are called neutral current interactions. SNO can measure the neutrino interactions through charged current or neutral current interactions.

Charged current interactions are only sensitive to ν_e while neutral current interactions are sensitive to all flavors. The neutrino flux inferred from the charged current events is about one-third of the flux from neutral current events, confirming the solar neutrino oscillation.

These oscillation results from solar, atmospheric, accelerator and long baseline reactor neutrino experiments can be explained very well by the model of three neutrino mixing. In this model, neutrinos interact or are produced in their weak eigenstates, which are not their mass eigenstates. In fact, the weak eigenstates are linear combinations of their mass eigenstates with definite masses. To be more specific, weak eigenstates can be obtained from mass eigenstates by a unitary transformation. As a neutrino propagates through space, the quantum mechanical phases of the three mass states evolve at slightly different rates due to the slight differences in the neutrino masses. This results in a changing mixture of mass states as the neutrino travels, but a different mixture of mass states corresponds to a different mixture of flavor states. The consequence is that after a flavor eigenstate is allowed to freely propagate in the space for some time, the mass eigenstate content changes. When the flavor is determined later on, the probability that it stays in the same original flavor is not 1, and there is some finite probability that it changes to other flavors. Since the neutrino flavor changes back and forth between different flavors when it propagates, the phenomenon is called neutrino oscillation. By studying the oscillation phenomenon, important parameters related to the transformation matrix or the states can be measured (see Section 2.2). There are three mixing angles θ_{12} , θ_{23} , θ_{13} and a CP-violating phase δ_{CP} pertaining to the mixing matrix. There are also three masses of the three mass eigenstates m_1 , m_2 and m_3 . However, most neutrino oscillation experiments are only sensitive to the mass squared splitting, $\Delta m_{ij}^2 \equiv m_i^2 - m_j^2$. By the time the Daya Bay neutrino experiment was designed, there was already precise knowledge in Δm_{21}^2 , the absolute value of $\Delta m_{31}^2 \approx \Delta m_{32}^2$, and the values of two mixing angles, θ_{12}

where $c_{ij} = \cos \theta_{ij}$, $s_{ij} = \sin \theta_{ij}$.

If an electron antineutrino $\bar{\nu}_e$ is produced at the source and propagates in space, at a distance L away from the source the survival probability, i.e. the probability that the neutrino doesn't change to other flavors, is

$$P(\bar{\nu}_e \rightarrow \bar{\nu}_e) = 1 - c_{13}^4 \sin^2 2\theta_{12} \sin^2 \Delta_{21} - c_{12}^2 \sin^2 2\theta_{13} \sin^2 \Delta_{31} - s_{12}^2 \sin^2 2\theta_{13} \sin^2 \Delta_{32} \quad (2.4)$$

where

$$\Delta_{jk} \equiv 1267 \Delta m_{jk}^2 (eV^2) \times \frac{L(km)}{E(MeV)} \quad (2.5)$$

$$\Delta m_{jk}^2 \equiv m_j^2 - m_k^2 \quad (2.6)$$

Among the three mixing angles θ_{13} was the only unknown parameter [12], and the goal of Daya Bay experiment at the time of the proposal was to measure $\sin^2 2\theta_{13}$ with 0.01 sensitivity at 90% confidence level.

2.2.2 Neutrino Flux and Energy Spectrum

Nuclear power is generated by fission reactions mainly from 4 kinds of isotopes, namely ^{235}U , ^{239}Pu , ^{238}U , and ^{241}Pu [13]. The fission products undergo beta decay and generate neutrinos as a by-product. Each fission reaction on average produces about 6 neutrinos. The detailed neutrino flux and energy spectrum at a particular time depend on the relative abundances of the isotopes, the total reactor thermal power, the fission rate of individual isotopes and the spectrum of the individual isotopes. The number of neutrinos released

isotope	e_i (MeV/fission)
^{235}U	201.92 ± 0.46
^{238}U	205.52 ± 0.96
^{239}Pu	209.99 ± 0.60
^{241}Pu	213.60 ± 0.65

Table 2.1: Typical thermal fission energy e_i at the midpoint of the reactor operation period.

by the reactor per unit time is

$$\phi(E) = \frac{W_{th}}{\sum_{i=1}^4 f_i e_i} \sum_{i=1}^4 f_i S_i(E) \quad (2.7)$$

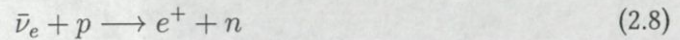
where i runs over the four main isotopes, W_{th} is the total thermal power, f_i is the fission fraction, e_i is the fission energy release and $S_i(E)$ is the neutrino energy spectrum. 3 ↩

The fission fraction of each isotope and the total thermal power are monitored and the weekly averaged numbers are offered by the nuclear power plant. e_i is the part of the fission energy that converts into heat. Typical values at the midpoint of the reactor operation period is given in Table 2.1 [13].

The antineutrino spectra $S_i(E)$ can be calculated from measured beta spectra. A three parameter parameterization was done by Vogel and Engel [14]. Figure 2.1 shows the spectra of the four dominant isotopes. ^{238}U produces the most antineutrinos per fission while ^{239}Pu produces the least.

2.2.3 $\bar{\nu}_e$ Detection

Daya Bay utilizes the renowned Cowan–Reines method of prompt-delayed coincidence to detect $\bar{\nu}_e$. The reaction involved in this method is the inverse beta decay (IBD),



cussion we use 404 days of data acquired in the 8-AD period combined with all 217 days of data acquired in the 6-AD period. Each AD has one measurement of number of IBD events. Meanwhile for each AD, one expected, i.e., no oscillation, ^{the}
^{number of IBD events} which is a function of $\sin^2 2\theta_{13}$ can be calculated. By measuring the number of IBD events and writing the expected number of IBD events as a function of θ_{13} one can construct a χ^2 function and through minimization θ_{13} can be estimated.

We will adopt a convention that the subscript c runs through reactor cores and d runs through antineutrino detectors. We want to know the expected number of IBD events for each AD, T_d . First we calculate the expected number of IBD events *without* oscillation N_d ,

$$N_d = \sum_{c=1}^6 \epsilon_d N_d^p \int \sigma(E) \frac{\phi_c(E)}{4\pi L_{cd}^2} dE \quad (2.11)$$

where N_d^p is the target number density of the d th detector, E is the neutrino energy, $\sigma(E)$ is the inverse beta decay total cross section, $\phi_c(E)$ is the neutrino flux from core c and L_{cd} is the baseline from core c to detector d . The IBD total cross section is given in [15]. The flux from core c is given by Equation 2.7 and depends on the instantaneous total thermal power of the reactor core which in general has a core to core difference. The detailed total thermal power is supplied by the nuclear power plant on a daily basis [16]. The baselines are measured by GPS with a precision of 28 mm [17]. The target masses are measured by load cells with a precision of 0.015%. By putting all the information together, the expected IBD events without oscillation can be obtained. Now if we assume the fluxes from all cores have the same energy functional form and only differ in magnitude, $\phi_c = f_c \phi$, then Equation 2.11 simplifies to

$$N_d = \sum_{c=1}^6 \epsilon_d N_d^p f_c \int \sigma(E) \frac{\phi(E)}{4\pi L_{cd}^2} dE \quad (2.12)$$

The expected number of IBD events *with* oscillation T_d is

$$T_d = \sum_{c=1}^6 \epsilon_d N_d^p f_c \int \sigma(E) P(\theta_{13}, L_{cd}, E) \frac{\phi(E)}{4\pi L_{cd}^2} dE \quad (2.13)$$

The only difference from Equation 2.12 is the insertion of the neutrino survival probability, which is given by

$$P(\theta_{13}, L_{cd}, E) = 1 - \sin^2 2\theta_{13} \sin^2(1.267 \Delta m_{32}^2 L_{cd}/E) \quad (2.14)$$

Here we have used $\Delta m_{31}^2 = 2.32_{-0.08}^{+0.12} \times 10^{-3} eV^2 \approx \Delta m_{32}^2$ and kept only the leading term at Daya Bay's baseline. Substituting Equation 2.14 back to Equation 2.13, we have

$$T_d = N_d - \sin^2 2\theta_{13} \frac{N_d^p}{4\pi} \sum_c \frac{f_c}{L_{cd}^2} \int \sigma \sin^2 \left(\frac{1.267 \Delta m_{32}^2 L_{cd}}{E} \right) \phi dE \quad (2.15)$$

If we define weight by

$$\omega_{cd} = \frac{f_c / L_{cd}^2}{\sum_c f_c / L_{cd}^2} \quad (2.16)$$

and oscillation factor by

$$\Delta_{cd} = \frac{\int \sigma \sin^2 \left(\frac{1.267 \Delta m_{32}^2 L_{cd}}{E} \right) \phi dE}{\int \sigma \phi dE} \quad (2.17)$$

and divide Equation 2.15 by N_d , we arrive at the result

$$\frac{T_d}{N_d} = 1 - \sin^2 2\theta_{13} \sum_c \omega_{cd} \Delta_{cd} \quad (2.18)$$

N_d was calculated previously, and ω_{cd} and Δ_{cd} can also be calculated from available data, so T_d can be expressed as a function of the one parameter to be estimated, namely $\sin^2 2\theta_{13}$.

If we call the second term in Equation 2.18 oscillation deficit, the result in ~~this~~ data taking 

these

AD1	AD2	AD3	AD4	AD5	AD6
$0.148\sin^2 2\theta_{13}$	$0.145\sin^2 2\theta_{13}$	$0.20\sin^2 2\theta_{13}$	$0.77\sin^2 2\theta_{13}$	$0.77\sin^2 2\theta_{13}$	$0.77\sin^2 2\theta_{13}$

Table 2.2: Oscillation deficit for six ADs

detector	AD1	AD2	AD3	AD4	AD5	AD6
IBD candidates	28935	28975	22466	3528	3436	3452
total backgrounds	556.19	441	358	145	148	139

Table 2.3: IBD analysis results

period is shown in Table 2.2.

Table 2.3 shows the analysis results of number of IBD candidates and total backgrounds. Table 2.4 shows the number of measured IBD events with background subtracted, the number of predicted IBD events *without* oscillation, and the ratio of the two numbers. A heuristic way to estimate $\sin^2 2\theta_{13}$ is to take the ratios from any 2 ADs, form the difference, and compare with the same difference with numbers taken from Table 2.2. For example if we take AD1 and AD6, we have $(0.77 - 0.148) \sin^2 2\theta_{13} = 101\% - 94.8\%$, or $\sin^2 2\theta_{13} = 0.099$.

Another way to estimate $\sin^2 2\theta_{13}$ is to use the so called “relative measurement” [18], i.e. by forming the ratio of two IBD rates registered by two different detectors. By this way we don’t have to rely on the absolute calculation of N_d and the systematic uncertainties concerning to the absolute reactor flux will cancel when forming the ratio. To start with, we take one of the far site AD and denote quantities concerning to the AD by subscript $d = F$. Meanwhile we take a near site AD and denote quantities with subscript $d = N$.

detector	AD1	AD2	AD3	AD4	AD5	AD6
measured IBD number	28379	28418	22034	3354.3	3260.4	3286.1
predicted IBD number	28083	28522	21895	3496.3	3502.6	3466.3
measured/predicted	101.0%	99.6%	100.6%	95.9%	93.9%	94.8%

Table 2.4: ratio of number of measured and predicted IBD events.

take $F = AD4$ and $N = AD3$, we have

$$\frac{\bar{L}_F^2}{\bar{L}_N^2} = \frac{170.81}{22.462} \quad (2.25)$$

Now we want to estimate Δ .

$$\Delta = \left(\frac{T_F}{\epsilon_F} \right) / \left(\frac{T_N}{\epsilon_N} \right) \cdot \left(\frac{\bar{L}_F^2}{\bar{L}_N^2} \right) \quad (2.26)$$

Since the ratio of the number of IBD events is the same as the ratio of the IBD rates, Δ can also be written as

$$\Delta = \left(\frac{R_{IBD,F}}{R_{IBD,N}} \right) \cdot \left(\frac{\bar{L}_F^2}{\bar{L}_N^2} \right) \quad (2.27)$$

Here $R_{IBD,d}$ is the true IBD rate for detector d after efficiency correction. To obtain $R_{IBD,d}$ from Table 2.6, note that the background numbers are efficiency corrected. Therefore for a detector d ,

$$R_{IBD} = \frac{N_{IBDc}}{\epsilon_\mu \epsilon_m T_{life}} - R_{acc} - R_{fn} - R_{iso} - R_{AmC} - R_{^{13}C} \quad (2.28)$$

where N_{IBDc} is the number of IBD candidates, ϵ_μ is the muon veto cut efficiency, ϵ_m is the multiplicity cut efficiency, T_{life} is the DAQ life time, R_{acc} is the accidentals rate, R_{fn} is the fast neutron rate, R_{iso} is the ${}^9\text{Li}/{}^8\text{He}$ rate, R_{AmC} is the AmC correlated background rate and $R_{^{13}C}$ is the ${}^{13}\text{C}(\alpha, n){}^{16}\text{O}$ rate. This is how the numbers in the row “IBD rate(/day)” are obtained. Take the IBD rate numbers from AD3 for near detector and AD4 for far detector, we can obtain Δ ,

$$\Delta = \left(\frac{74.33}{601.77} \right) \left(\frac{170.81}{22.462} \right) = 0.939 \quad (2.29)$$

If we utilize IBD data from all four far site ADs, we have

$$\frac{\delta R_{IBD}^{stat}}{R_{IBD}} \approx \frac{1}{\sqrt{27000 \times 4}} \approx 0.003 \quad (2.35)$$

Thus

$$\delta(\sin^2 2\theta_{13})^{stat} = \frac{\delta \Delta^{stat}}{\Omega_F - \Delta \Omega_N} = \frac{\Delta \left(\frac{\delta R_{IBD}^{stat}}{R_{IBD}} \right)}{\Omega_F - \Delta \Omega_N} = \frac{0.939 \times 0.003}{0.6} = 0.005 \quad (2.36)$$

The systematic uncertainty right now is dominated by ${}^9\text{Li}/{}^8\text{He}$ background. When summed in quadrature, this term dominates,

$$\frac{R_{IBD}^{syst}}{R_{IBD}} \approx \frac{\delta R_{iso}}{R_{IBD}} \approx \frac{0.14}{74} \approx 0.002 \quad (2.37)$$

Thus

$$\delta(\sin^2 2\theta_{13})^{syst} = \frac{\delta \Delta^{syst}}{\Omega_F - \Delta \Omega_N} = \frac{\Delta \left(\frac{\delta R_{IBD}^{syst}}{R_{IBD}} \right)}{\Omega_F - \Delta \Omega_N} = \frac{0.939 \times 0.002}{0.6} = 0.003 \quad (2.38)$$

If Daya Bay keeps data taking, the statistical uncertainty will eventually go down to the same level as the systematic uncertainty. To reach a more precise value of θ_{13} , efforts have to be put into reducing the systematic uncertainties. Now the relative uncertainty in the fast neutron background is about 20%, which still has room for improvements. This study, interesting in its own right, may shed some light on reducing the systematic uncertainty in the fast neutron background.

2.5 Muon Induced Backgrounds

The Earth is constantly bombarded by high energy particles known as cosmic rays. The primary source of cosmic ray is protons. When protons interact with the air molecules, secondary particles originate which in turn decay and generate muons, neutrinos, electrons and photons. Figure 2.4 shows the vertical fluxes of the dominant cosmic ray components estimated from the intensity of primary nucleons incident on top of the atmosphere. At sea level (altitude = 0) there are still high fluxes of cosmic rays ranging from about 0.1 to $100 \text{ m}^{-2} \text{s}^{-1} \text{sr}^{-1}$ [10]. Fortunately rocks are very good natural shielding from the particles and when one goes deep enough underground only muons and neutrinos can survive. Therefore sensitive experiments go underground and the main sources of background would be the natural radioactivity from rocks as well as muons and particles or isotopes induced by muons.

Daya Bay's experimental halls are also underground, and the muon induced neutrons and isotopes constitute one of the major background sources. For Daya Bay, the sea level muon energy and angular distribution is important because in order to get the energy and angular distribution in each hall with Monte Carlo simulation, the sea level data together with the mountain overburden profile and the rock composition is input into the simulation and the muons are then propagated through the rock to get the propagated energy and angular distribution for those survived to the ceiling of the halls. Conventionally the sea level muon flux is described by the Geisser formula [19],

$$\frac{dN_\mu}{dE_\mu d\Omega} = \frac{0.14E_\mu^{-2.7}}{\text{cm}^2 \cdot \text{s} \cdot \text{sr} \cdot \text{GeV}} \left\{ \frac{1}{1 + \frac{1.1E_\mu \cos\theta}{115\text{GeV}}} + \frac{0.054}{1 + \frac{1.1E_\mu \cos\theta}{850\text{GeV}}} \right\} \quad (2.39)$$

where the two terms in the braces give the contribution of pions and kaons, respectively.

Chapter 3

The Daya Bay Experiment

3.1 The Daya Bay Site

To measure θ_{13} , an experimental site with reactors of high thermal power to supply large antineutrino flux and with mountains nearby to serve as cosmic ray shielding is required. Daya Bay is an appropriate site meeting the requirements.

The Daya Bay reactor complex is located on the southeast coast of China, 55 km north-east of Hong Kong. The reactor complex is composed of 3 nuclear power plants, namely the Daya Bay (DYB) nuclear power plant, the Ling Ao (LA) nuclear power plant, and the Ling Ao-II (LA II) nuclear power plant. Each nuclear power plant is equipped with a pair of functionally identical pressurized water reactors (PWR) separated by 90 m. Each reactor core supplies 2.9 GW thermal power. The last core going online started commercial operation in August, 2011. The Ling Ao nuclear power plant is ~1100 m from the Daya Bay nuclear power plant, and the Ling Ao-II is ~500 m from the Ling Ao.

The Daya Bay experimental facility is composed of 3 underground experimental halls, a surface assembly building, a liquid scintillator (LS) hall and a water hall (EH4). The underground halls are connected by horizontal tunnels. The 3 experimental halls are where

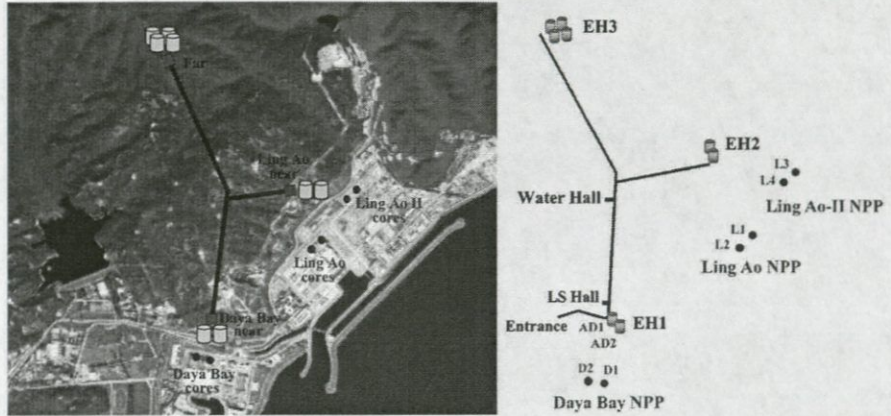


Figure 3.1: The Daya Bay site.

the antineutrino detectors and the muon detectors are installed. The experimental hall closest to the Daya Bay/Ling Ao nuclear power plant is called the Daya Bay/Ling Ao near site, or experimental hall 1/2 (EH1/EH2). The experimental hall farthest from all the reactor cores is called the Far site, or experimental hall 3 (EH3). The near sites are designed to hold two antineutrino detectors (ADs) each while the far site is designed to hold four ADs. The surface assembly building is the place where experimenters assemble the ADs, do the dry run tests, and other detector related work before transporting the equipment underground. The LS hall is where Daya Bay's liquid scintillator and Gd-doped liquid scintillator are produced, and is where the ADs are filled. The water hall is where the ultra-pure water system is placed which supplies ultra-pure water to the 3 water pools in EH1, EH2, and EH3. Figure 3.1 shows the experimental facility and the 6 reactor cores. The distances from the centroid of the reactor pairs to the sites are shown in Table 3.1. The Global Positioning System (GPS) and modern theodolites are utilized to survey all distances. The uncertainty of the baselines from the geometric center of the reactor cores to the AD centers was determined to be about 28 mm [20].

The overburden in equivalent meters of water (m.w.e.), simulated muon rate and average muon energy are listed in Table 3.2.

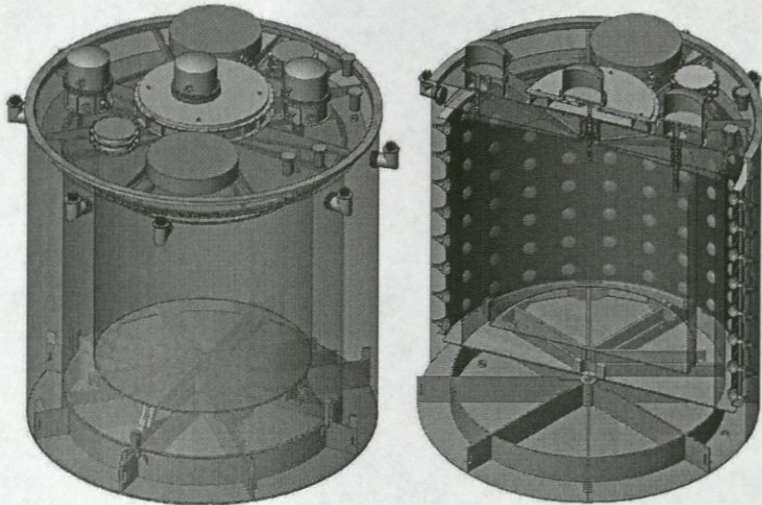


Figure 3.2: Cross sectional view of the Daya Bay antineutrino detector.

source	particle	frequency (Hz)
^{68}Ge	β^+	15
^{241}Am - ^{13}C and ^{60}Co	n	0.5
	γ	100
LED diffuser ball	light	500

Table 3.3: Sources in an ACU and their properties.

on 8 ladders along the circumference of the SSV and within the mineral oil region. The PMTs are arranged in 24 columns and 8 rings. Two specular reflectors are installed above and below the LS volume to increase the photo-coverage from 6% to 12%.

Three Automated Calibration Units (ACU-A, ACU-B, and ACU-C) are mounted on the top of the SSV of each AD as shown in Figure 3.3. Each ACU contains three sources which are listed in Table 3.3. The sources can be deployed to better than 0.5 cm along a vertical line down to the bottom of the acrylic vessels.

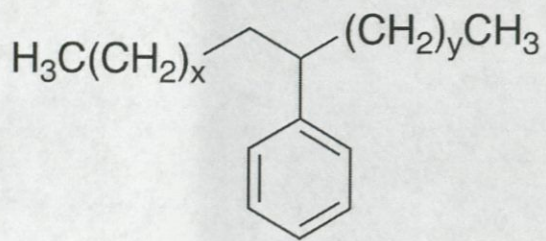


Figure 3.4: The Daya Bay liquid scintillator solvent, linear alkylbenzene (LAB).

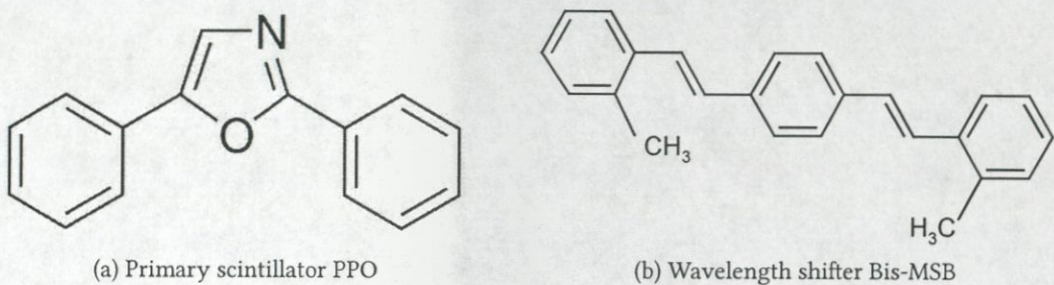


Figure 3.5: The primary scintillator and the wavelength shifter in Daya Bay's LS.

order of 10 m, high light yield, low radioactive impurities, and high flash point for safe operation. LAB's chemical composition is basically a straight alkyl chain of 10-13 carbons attached to a benzene ring (Figure 3.4). The LS also contains 3 g/L PPO and 15 mg/L Bis-MSB as the primary scintillator and the wavelength shifter, respectively (Figure 3.5a and Figure 3.5b).

Thermalized neutrons in the scintillator can be captured on hydrogen with a mean capture time of $\sim 200 \mu\text{s}$ and decay γ 's of 2.2 MeV. The doping of gadolinium causes neutron capture on Gd with a mean capture time of $\sim 30 \mu\text{s}$ and decay γ 's of 8 MeV. The shorter capture time greatly reduces the rate of accidental coincidence, and the 8 MeV energy is way above the natural radioactivity backgrounds. Besides, the neutron capture cross section on gadolinium is 49,000 barn, more than 10^5 times larger than the capture cross section on hydrogen (~ 0.3 barn). As a consequence, Daya Bay's target LS is doped with 0.1% Gd.

It is seen from Figure 3.5a that other than carbon and hydrogen, Daya Bay's scintil-

Chapter 4

The Daya Bay Data Acquisition

In this chapter the Daya Bay data processing from acquisition to analysis is introduced. First, the Daya Bay electronics is described, followed by the data acquisition and data transfer to the United States. Then Daya Bay's data quality, in particular the background due to the flasher PMTs, is discussed. After data quality the Daya Bay offline software, "NuWa", is introduced, and the official production data are described.

4.1 Trigger and Readout

Each detector subsystem (AD, IWS, OWS, RPC) has its own readout electronics and is housed in different VME (Versa Module Europa) crates [28]. VME bus is a bus system which makes use of the Eurocard standard, and is widely adopted in high energy physics experiments¹. PMT based detectors have physically identical readout crates with the only difference in the number of PMT channels. The raw signals from PMTs are sent to the front-end electronic boards (FEEs) which sum the charge from all sixteen input channels, identify over-threshold channels, and record their timing and charge in a buffer on the board with a 40 MHz sampling rate. The FEE sends the number of channels above thresh-

¹For example, see the CAEN website.

old and the sum of charges from all the channels to the trigger system. If a trigger is issued, the FEE reads out the charge and timing within $1 \mu\text{s}$ for every over-threshold channel. In the mean time the charge and timing within 100 ns just before the over-threshold instant are also read out for the electronics baseline study. There are primarily two kinds of trigger modes, the so-called NHIT mode which counts the number of over-threshold PMTs and the E-Sum mode which sums the total charge of all the channels of a FEE [29].
Triggers can be issued by either mode or by requiring both. The trigger system can also accept external triggers such as those from the calibration system. The trigger system blocks triggers when either the trigger data buffer or the FEE data buffer is almost full. The blocked triggers are recorded for calculating the dead time offline.

4.2 Flasher PMTs

Daya Bay observed that a small number of PMTs emit light spontaneously probably caused by the discharge in the PMT base [24]. These are known as flasher events. For Daya Bay, the reconstructed energy of a flasher event spans a broad range, from sub-MeV up to 100 MeV. The flasher events have very distinctive signatures which can be used to reject them effectively. For one thing, the flashing PMT has a high fraction of total charge. For the other, the PMTs to the opposite side of the flashing PMT see excessive light. The charge pattern in an AD of a typical flasher event is shown in Figure 4.1. To reject the flasher events, two variables are constructed, namely $MaxQ$ and $Quad$. $MaxQ$ is the largest fraction of the total detected charge seen by a single PMT. After the identification of the $MaxQ$ and the PMT corresponding to $MaxQ$, the 24 columns of PMTs are divided into four even quadrants, with the PMT with the largest charge fraction sitting in the center of the quadrant which is called Quadrant 1. Then viewed from top, the remaining quadrants are named Quadrant 2, Quadrant 3, and Quadrant 4 clockwise. The variable $Quad$ is

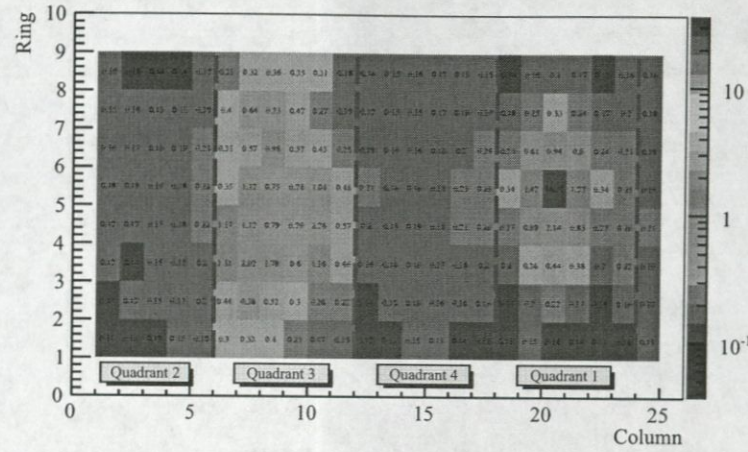


Figure 4.1: A typical flasher event with the flashing PMT in column 20 row 5 and the PMTs across the AD with high charge.

defined as $Q_3/(Q_2 + Q_4)$, where Q_i is the total charge in the i th quadrant. It is found that the flasher events satisfy the inequality

$$\left(\frac{\text{Max}Q}{0.45}\right)^2 + (\text{Quad})^2 > 1 \quad (4.1)$$

The discrimination power of this cut decreases with energy. For events with values very close to 1, careful studies are conducted, and it is found that the IBD inefficiency due to this flasher cut is $(0.02 \pm 0.01)\%$ [17]. The flasher contamination in the IBD selection is estimated to be $< 10^{-4}$. In addition, flasher events which survived the flasher cut would eventually be removed by the accidental background cut. Due to the high efficiency of this flasher cut, all PMTs are in operation during data taking including the flashing PMTs. In this study, all events are required to pass the flasher cut before further analysis.

4.3 Data Storage and Transfer

The raw data recorded by the DAQ system are first transferred to the Daya Bay onsite storage disks. The Performance Quality Monitoring (PQM) system [30] then uses this ↙

these ↖

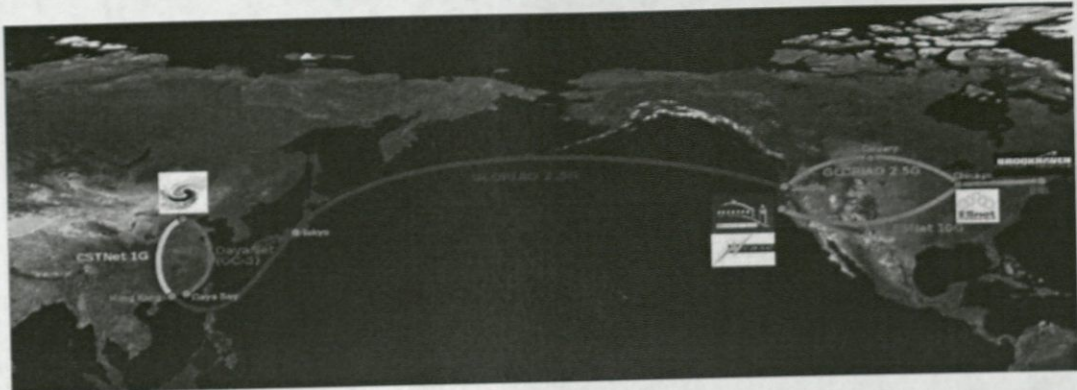


Figure 4.2: Data transfer from Daya Bay onsite to IHEP and from IHEP to LBNL.

onsite data combined with the onsite database to produce data for online data quality check. The raw data are then transferred to the lxslc5 cluster of the Institute of High Energy Physics (IHEP) in Beijing, which in turn are transferred to the PDSF cluster of the Lawrence Berkeley National Laboratory (LBNL) for storage in the U.S.. The data route from the onsite storage to the data warehouses is shown in Figure 4.2. The raw data at IHEP and LBNL are processed to produce the so called “Keep Up Production” (KUP) data to be used by the Offline Data Monitor (ODM) system, providing offline data quality check². A Data Quality (DQ) database is constructed based on the KUP data to mark datasets with good or bad data quality.

The data transfer between the onsite and the IHEP and LBNL clusters is done with a piece of management software called SPADE. SPADE stands for South Pole Archival and Data Exchange, originally developed by IceCube and adopted by Daya Bay [31]. The design goal of SPADE is to reliably transfer data from an experiment to its data warehouse. What SPADE does is that it scans the local clusters for new files, transfers a copy to the data warehouse, and deletes the local copy. There are several advantages of employing SPADE. SPADE handles network downtime and includes bookkeeping of data movement. The adoption of SPADE by Daya Bay required only slight modifications, and SPADE has

²<https://portal-auth.nersc.gov/dayabay/odm>

After that the disk-shaped polycarbonate spacers were glued to the same side without graphite coating in a $10\text{ cm} \times 10\text{ cm}$ grid, another bakelite sheet was glued on top of the spacers to form a chamber. In the first 2 hours after the chamber was sealed, the pressure in the chamber was lowered to about 8% atmospheric pressure to ensure good glue cure. A $< 0.1\%$ leak rate was required, and failed RPCs were glued again along the perimeter and tested again. Finally for each gas feedthrough a high voltage pin was soldered inside and made contact with the copper tape. The exposed copper tape and solder were then covered by insulating epoxy.

Newly-made RPCs usually have a noise rate so high that it lowers the efficiency. It is known [39] that a so-called training process can bring the noise down to a stable and acceptable rate. The training is done by applying the high voltage on RPC up to 10 kV for at least 48 hours, and flowing pure argon without other quenching gas so that the current can reach 2-3 orders of magnitude higher than that of normal operation condition. The training process burns off dust and “polishes” the surfaces. Figure 5.2 shows the training current of a sample of 7 RPCs. We see that the current rises in the beginning and then drops off to a steady value. After training, when the RPC is put to use and operated in normal condition, the current is usually reduced by a factor of 10 compared with RPCs which are not trained.

*(1) not needed
after 15'*

5.2 RPC Modules

The RPC arrays in EH1 and EH2 are composed of $6\text{ rows} \times 9\text{ columns}$ of RPC modules while that in EH3 is composed of $9\text{ rows} \times 9\text{ columns}$ of RPC modules. Each module is an aluminum box of dimensions $2.17\text{m} \times 2.20\text{m} \times 0.08\text{m}$ containing bare chambers, insulating materials, support panels, readout strips, and ground planes. The RPC modules sit on the support structure which can be moved to an “RPC hall” next to the water pool

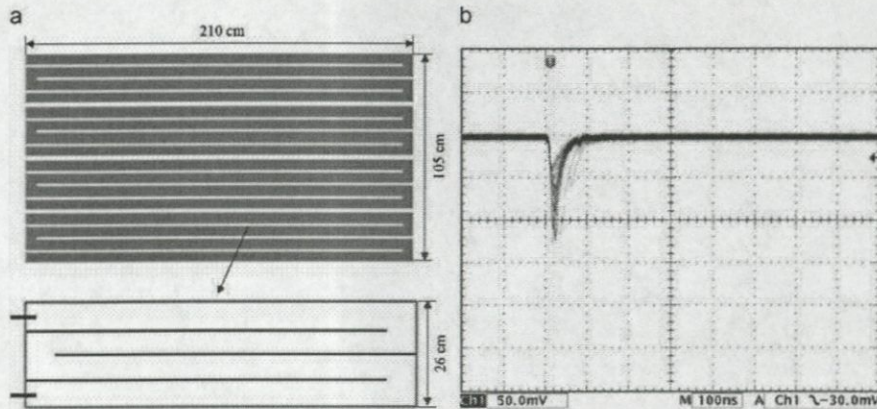


Figure 5.5: (a) Readout zigzag structure and the signal termination. (b) Readout signals on the oscilloscope.

long (see bottom right of Figure 5.4). The zigzag design in effect changes the impedance so as to give a larger and narrower pulse because of the change in the impedance of the transmission line [40]. One end of the strip is connected to the RPC Front End Card (FEC, see Section 5.4) while the other end is connected to a ground by two $27\ \Omega$ resistors, a value determined in bench tests (see Figure 5.5(a)). Figure 5.5(b) shows some signals read out by the oscilloscope in bench tests. The signal threshold in Daya Bay's physics data taking is set at 30 mV. The 4 readout layers are oriented, from bottom to top, in the x , y , y , x directions as shown in Figure 5.4. With this readout arrangement, the position of the incident muon can be determined by identifying the intersection of the x and y strips.

5.3 Gas and High Voltage System

The RPCs operate in streamer mode with a gas mixture of Ar:C₂H₂F₄:i-C₄H₁₀:SF₆=65.5:30:4:0.5. Each site has a gas system which consists of gas cylinders, gas mixing and distribution systems, fire safety monitoring systems, and gas chromatography (GC) systems. The flow rate of each site is about 1 RPC volume exchange per day, and is controlled by an electronic mass flow control system.

board or module	near hall	far hall
FEC	54	81
ROT	4	6
ROM	1	1
RTM	1	1

Table 5.1: Number of boards/modules installed in each hall.

pass them to ROT. Signal transmission from FEC to ROT is done with flat cables. There are two kinds of local trigger modes, 2/4 and 3/4. In 2/4 mode, triggers are issued if at least two layers of RPCs are fired. In 3/4 mode, triggers are issued if at least three layers of RPCs are fired. In Daya Bay’s physics data taking, since the amount of data generated by 2/4 mode takes too much storage and is mostly due to non-physics events, 3/4 trigger mode is used. The ROT transmits readout data and configuration data between FEC and ROM. In addition, ROT transmits local trigger signals to RTM. Each ROT accepts up to 15 FEC signals, packs up data from 15 cards, and passes them to ROM and RTM through optical links. The ROM and RTM then process the data and issue triggers.

5.5 Event Reconstruction

In this study the yield of muon-induced neutrons is measured by constructing fiducial volumes around the muon tracks. Only neutrons captured inside the fiducial volume are counted. In this section the event vertices and the muon tracks are discussed.

5.5.1 AD Event Reconstruction

In this study, the energy and vertex of an AD event are obtained by the “AdSimple” reconstruction algorithm [41]. AdSimple reconstructs the energy and vertex of a point-like event such as the neutron capture on Gd.

Vertex Reconstruction The vertex reconstruction in AdSimple involves two steps. First the charge-weighted mean from all PMTs is used to obtain the preliminary value. Then a correction scheme obtained from MC simulation is applied to the preliminary value. The preliminary vertex is obtained by

$$\vec{r}_{coc} = \frac{\sum_i Q_i \vec{r}_i}{\sum_i Q_i} \quad (5.2)$$

where \vec{r}_{coc} is the center of charge position, i runs over all 192 8" PMTs, Q_i is the charge received by the i th PMT, and \vec{r}_i is the position of the PMT. As a result of reflectors on the top and bottom of the AD, it is found that the the center of charge positions \vec{r}_{coc} are pulled to the center of the AD. This bias can be corrected by the IBD Monte Carlo simulation including both positron and neutron events. The OAV is divided into bins in both the radial ρ and the vertical z directions. Then quantities $\Delta\rho$ and Δz are defined¹ representing the deviation of \vec{r}_{coc} from the true position \vec{r}_{true} . For each bin the average values of $\Delta\rho$ and Δz are calculated, and these values are assigned to the center of the bin. To obtain $(\Delta\rho, \Delta z)$ for all (ρ, z) , an interpolation is applied. Finally the correction is added to each \vec{r}_{coc} to obtain the reconstructed vertex \vec{r}_{rec} . The position resolution of this algorithm for Gd captured neutrons is ~ 20 cm in both ρ and z directions.

Energy Reconstruction The AdSimple energy reconstruction involves three steps. The first step is the determination of the total charge deposited in the detector recorded by PMTs. The second step is the conversion of this charge to a physical energy scale. Fi-

¹

$$\Delta\rho = \vec{r}_{true} \cdot \frac{\vec{r}_{coc}}{\rho_{coc}} - \rho_{coc} \quad (5.3)$$

$$\Delta z = z_{true} - z_{coc} \quad (5.4)$$

try not
to split

Finally a correction is applied to account for the detector non-uniformity. Concerning the total charge determination, for an AD trigger the energies deposited in all PMTs are all counted. For each PMT, the pedestal subtracted ADC value is converted into number of photoelectrons (pe's) using the calibration constants specific to individual channels in the offline database which is updated weekly. Only PMT hits in the time window $[-1650\text{ns}, -1250\text{ns}]$ with respect to the time the trigger is issued are summed to obtain the PMT charge for each PMT.

Once the total charge sum is obtained for an AD trigger in the units of photoelectrons, the charge has to be converted into real physical energy scale. Here the spallation neutrons are used to set the photoelectron to energy scale. The spallation neutrons captured on Gd is uniformly distributed in the GdLS, providing access to the whole detector active volume. The 8 MeV peak is close to the lower bound of the delayed signal energy cut which constitute a dominant systematic uncertainty. The number of photoelectrons divided by 8 MeV then serves as the energy scale constant for the AD. For all ADs, this value is about 170 photoelectrons/MeV. Finally the energy scale as a function of r and z are studied and corrected.

In this study, muon-induced neutrons are selected by an energy cut with energies reconstructed by AdSimple algorithm. Also, the capture sites of neutrons are required to be within a fiducial volume with capture vertices reconstructed by this algorithm as well.

5.5.2 Muon Track Reconstruction

In this study, muon tracks are reconstructed by the muon system. The muon system consists of three independent detectors, the RPC, the IWS, and the OWS. The RPC by design can reconstruct the muon incident position simply by identifying the intersection of the fired strips which gives a point in the muon track. On the other hand the two PMT based Cherenkov detectors can each offer a reconstructed point in the muon track by

to improve. This algorithm uses only the PMT charge and hit pattern to reconstruct the muon track, and it turns out to have a reasonably good resolution.

As in the AD vertex reconstruction, a charge weighted mean is used as the reconstructed vertex,

$$\vec{r}_{rec} = \frac{\sum_{i=1}^{n_{max}} Q_i \vec{r}_i}{\sum_{i=1}^{n_{max}} Q_i} \quad (5.5)$$

where Q_i is the charge the i th PMT receives, and \vec{r}_i is the position vector of that PMT. n_{max} is the first n_{max} PMTs with the largest received charge, and is determined by simulation. The idea is that the closer the PMT is to the muon track the more light it will receive. Also since the Cherenkov radiation is directional, the PMTs in proximity to the PMT with largest charge receive more light than PMTs far from the muon track. Therefore only selecting a number of PMTs with ^{the} largest charge provides better resolution than taking all PMTs in the pool. Since each water pool is regarded as an independent detector, this algorithm gives two reconstructed vertices, one for each pool.

The resolution of this algorithm is obtained by simulation. One can determine the distance from the center of the OWS to the true track. Call this parameter d_{true} . The same point to the reconstructed track is d_{rec} . One can plot the distribution of $d_{rec} - d_{true}$. The position resolution obtained from the distribution is ~ 60 cm shown in Figure 5.8.

5.5.2.3 Muon Track Reconstruction

When a muon passes through the Daya Bay muon system, depending on the geometry of the track and the muon detectors, at most four points can be reconstructed if the telescope RPC is also hit by the muon. Since RPCs have a superior resolution than the water pool, in this study only muons having an RPC trigger and a water pool vertex are considered. Furthermore, since ADs are sitting in the inner water pool, the PMTs on the bottom of the pool are shadowed by the ADs. This situation known as the AD shadowing effect. The

α and β still remain. The Daya Bay experiment has three experimental halls each with different overburden. Therefore, Daya Bay, a single experiment, can measure three yield values corresponding to three different mean muon energies.

There are therefore 8 terms to be determined in order to measure the yield as a function of the mean muon energy, namely N_n^s , ϵ_{Gd} , ϵ_E , ϵ_T , ϵ_{acc} , L , ρ and \bar{E}_μ . In the following sections each term and its uncertainty will be discussed in detail. 

The discussion will start with more widely studied quantities and move on to the quantities more specific to this study.

7.3.1 Target Density ρ

The GdLS density is [60]

$$\rho = 0.861 \pm 0.001 \text{ g/cm}^3 \quad (7.7)$$

7.3.2 Gd Capture Ratio ϵ_{Gd}

Spallation neutrons generated in the target mass, GdLS, may not all be captured on Gd. Some could be captured on H or other nuclei. Some are not captured at all and leave the detector which we call spill-out neutrons. There are also spill-in neutrons, namely neutrons generated outside and transported into the fiducial volume and get captured on Gd. Since in this study we select only the Gd captured neutrons, we have to determine this efficiency which is often called the Gd capture ratio. 

Many studies had been done on the Gd capture ratio with spallation neutrons [61] [62] [63], calibration sources [61] [63], special calibration runs [64] [65] [66] [67] [68] and Monte Carlo simulation [69]. However, different studies adopt slightly different definitions of 

this ratio. Here we define the Gd capture ratio as

$$\epsilon_{Gd} = \frac{\text{number of neutrons generated in GdLS and captured on Gd}}{\text{number of neutrons generated in GdLS}} \quad (7.8)$$

We use the more up-to-date study [68]. In this study a complete comparison between AmC, AmBe, PuC and Monte Carlo is given and the efficiency due to energy cuts is corrected for resulting in a ϵ_{Gd} definition which coincides with Eq. 7.8. The final result is quoted as,

$$\epsilon_{Gd} = 85.2\% \pm 0.4\% \quad (7.9)$$

7.3.3 Energy Cut Efficiency ϵ_E

One of the signatures of a neutron captured on Gd is the 8 MeV γ energy released from the de-excitation of Gd^* . Therefore, we use the 8 MeV energy cut efficiency published in the IBD analysis [20], combining the correlated and uncorrelated uncertainties,

$$\epsilon_E = 90.9\% \pm 0.61\% \quad (7.10)$$

7.3.4 Capture Time Cut Efficiency ϵ_T

The other signature of a neutron captured on Gd is the capture time whose mean value is $\sim 28\mu s$. Figure 7.2 shows the IBD neutron capture time distribution. The distribution is not a simple exponential but has a rising edge in the beginning of the spectrum. A 2-exponential fit to model the whole spectrum [70], one of which accounts for the rising edge due to the thermalization of neutrons.

In the spallation neutron case, there are several differences. First, the initial energy of the spallation neutrons can be higher than the IBD neutrons, leading to a longer thermalization time. Second, after the muon passes through the AD, the huge amount of energy

7.3.6 Lateral Acceptance ϵ_{acc}

The neutrons are expected to be boosted forward. There is space before the fiducial cylinder. If neutrons are produced upstream, they enter the cylinder even if they are not produced inside. As a result, the neutron flux entering the fiducial cylinder from upstream of the track equals the neutron flux leaving the fiducial cylinder. We only need the lateral distribution to determine the detector acceptance. Figure 7.6 shows the distribution of the relative longitudinal position of the capture point relative to the cylinder center. It clearly shows a uniform distribution, which shows spill-in equals spill-out in the longitudinal direction.

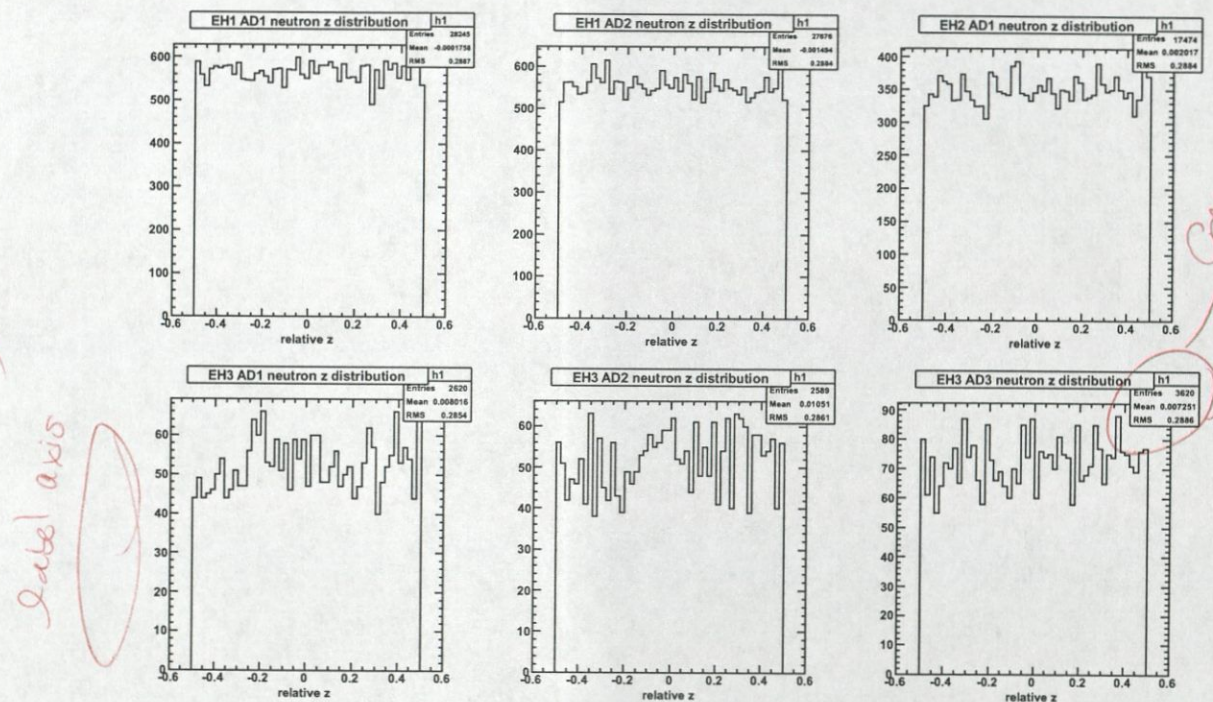


Figure 7.6: Relative longitudinal capture position with respect to the fiducial cylinder center.

To estimate the lateral acceptance due to the finite volume of the fiducial cylinders, we lift the muon selection criteria that a fiducial cylinder is able to be constructed. This mean we practically use every muons which have a track reconstructible by RPC-OWS

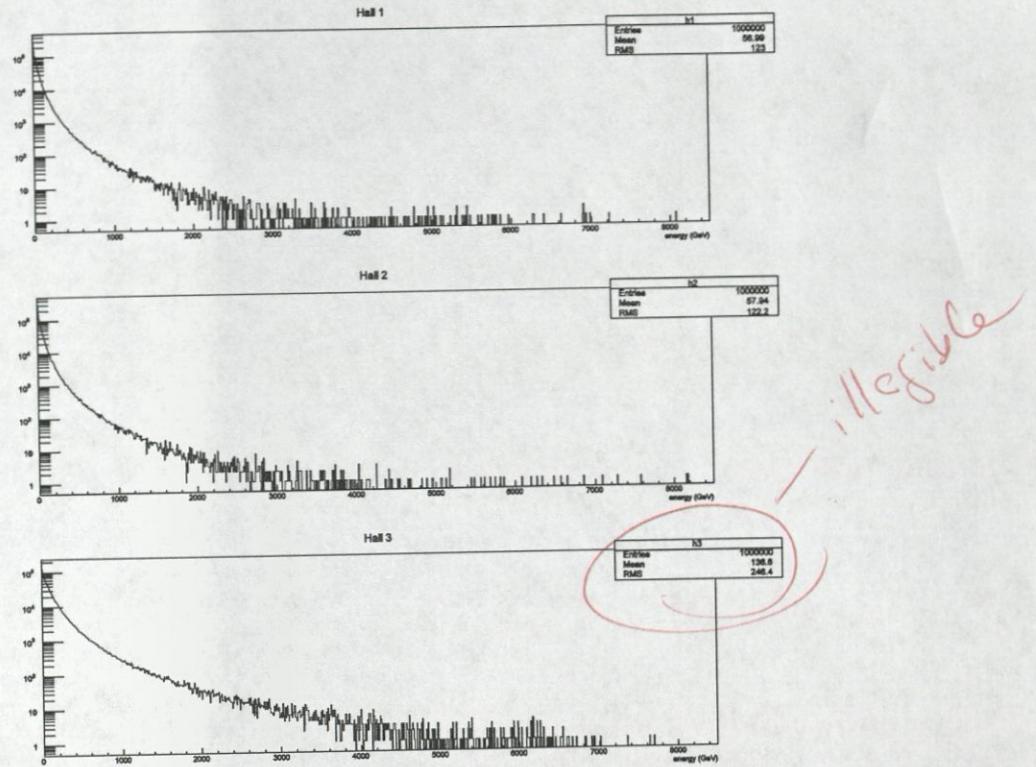


Figure 7.8: Simulated muon energy spectra in the three halls.

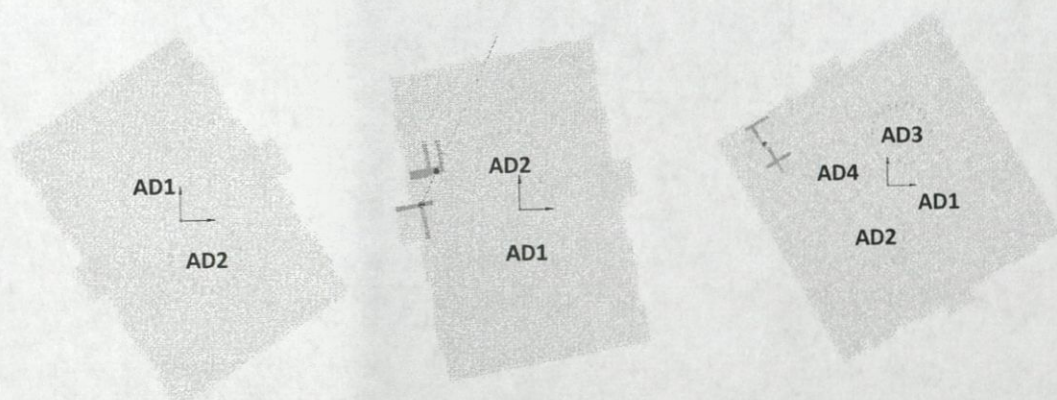


Figure 7.9: RPC coverage for each AD in different halls.

detector	mean muon energy (GeV)
EH1 AD1	47 ± 2
EH1 AD2	47 ± 2
EH2 AD1	50 ± 2
EH3 AD1	123 ± 6
EH3 AD2	130 ± 7
EH3 AD3	127 ± 6

Table 7.6: Mean muon energy seen by each AD.

7.3.8 Results

Applying the error propagation formula to the terms, assuming the terms N_n^s/L , ϵ_E , ϵ_T , ϵ_{Gd} , ϵ_{acc} , ρ are independent, the total systematic uncertainty can be combined in quadrature

ture

$$\left(\frac{\sigma_{Y_n}^{syst}}{Y_n} \right)^2 = \left(\frac{\sigma_{N_n^s/L}^{syst}}{N_n^s/L} \right)^2 + \left(\frac{\sigma_{\epsilon_E}}{\epsilon_E} \right)^2 + \left(\frac{\sigma_{\epsilon_T}}{\epsilon_T} \right)^2 + \left(\frac{\sigma_{\epsilon_{Gd}}}{\epsilon_{Gd}} \right)^2 + \left(\frac{\sigma_{\epsilon_{acc}}}{\epsilon_{acc}} \right)^2 + \left(\frac{\sigma_\rho}{\rho} \right)^2 \quad (7.13)$$

Also the N_n^s contains the statistical uncertainty

$$\left(\frac{\sigma_{Y_n}^{stat}}{Y_n} \right)^2 = \left(\frac{\sigma_{N_n^s}}{N_n^s} \right)^2 \quad (7.14)$$

The relative systematic and statistical uncertainties are summarized in Tables 7.7 and 7.8.

The total uncertainty is again, obtained by quadrature

term	N_n^s/L	ϵ_E	ϵ_T	ϵ_{Gd}	ϵ_{acc}	ρ
value (%)	10	0.7	5	0.5	10	0.1

Table 7.7: Relative systematic uncertainties for terms in the yield formula.

detector	EH1 AD1	EH1 AD2	EH2 AD1	EH3 AD1	EH3 AD2	EH3 AD3
value (%)	0.6	0.6	0.8	2	2	2

Table 7.8: Relative statistical uncertainties for each AD.

Chapter 8

Conclusion

The Daya Bay Reactor Neutrino Experiment is a precision measurement of θ_{13} designed to measure $\sin^2 2\theta_{13}$ with sensitivity < 0.01 at 90% confidence level. In 2012 Daya Bay discovered that θ_{13} is nonzero with 5.2σ and $\sin^2 2\theta_{13} = 0.092 \pm 0.016(\text{stat.}) \pm 0.005(\text{syst.})$ [20]. The fast neutron background constitutes one of the five backgrounds in θ_{13} measurement. Therefore understanding the neutron yield induced by cosmic ray muons is important.

In this study we make a well-defined cylindrical fiducial volume of fixed radius around each muon track. Only neutrons captured in the fiducial volume is counted. We use the lateral distribution of the neutron captured position to correct for the inefficiency due to the neutrons leaking out of the fiducial volume.

The muon tracks are reconstructed by connecting the RPC and OWS reconstructed points. The RPC positions are reconstructed by the centroids of the fired x and y strips with a resolution of ~ 7 cm. The OWS positions are reconstructed by the charge-weighted mean of the positions of fired PMTs whose resolution is ~ 60 cm. The neutron captured positions are reconstructed by charge-weighted mean corrected by Monte Carlo simulation with a resolution of ~ 20 cm. The resolutions of the reconstruction algorithms are used for estimating errors in the neutron yield determination. Details in constructing the

check
usager de (-)
si mante consistant ✓

Appendix A

Geometric Problems Related to Muon Physics at Daya Bay

Run on

The Daya Bay neutrino experiment is equipped with excellent muon tracker detectors, more aspects of the muon physics can be studied by reconstructing muon tracks. Since in each collision the muon deflection is usually small, the muon track is usually approximated by a straight line. Besides, detectors usually are of regular shapes such as being spherical or cylindrical, they can be modeled by simple 3D algebraic equations. There are several interesting questions concerning to the relations between different geometric objects and in this appendix simple solutions to these pure analytic geometry problems are presented.

thus ?

A.1 Track Length in a Cylinder

At Daya Bay the deposited energy of each muon is registered. Since the ionization energy loss is roughly proportional to the track length the muon traverses, track length is also a quantity of interest. Because the energy registered by the detector is mainly from the

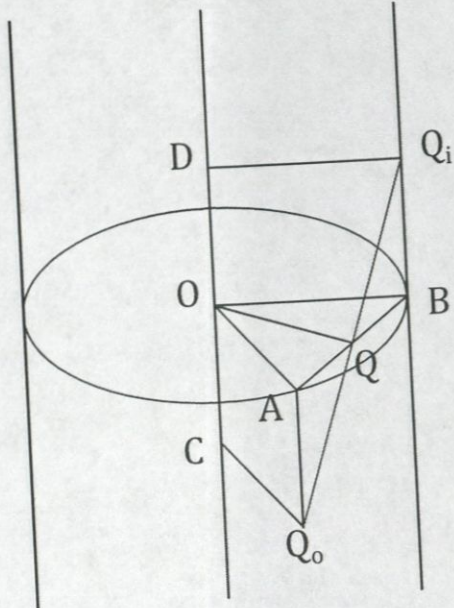


Figure A.1: An illustration of a cylinder and a straight line passing through it. Given points O and Q , we want to find Q_i and Q_o .

$\vec{v}_c \cdot (\vec{v} \times \vec{n}) = (\vec{v}_c \times \vec{v}) \cdot \vec{n} = -n^2$. Then we get

$$t = \vec{v}_c \cdot (\vec{p}_r \times \vec{n}) / n^2 \quad (\text{A.8})$$

Similarly we can dot Equation A.7 with \vec{v} to obtain t_c .

Now that we have the shortest distance between the skew lines and the corresponding points, we are ready to solve for the intersection points. Figure A.1 shows a cylinder in blue and a straight line in red passing through it. \overleftrightarrow{CD} is the cylinder axis and $\overleftrightarrow{Q_iQ_o}$ is the track line. Given the closest points O , Q and angle $\angle QQ_iB = \angle QQ_oA = \theta$, we want to find $\ell = \overline{QQ_i} = \overline{QQ_o}$.

ℓ can actually be found by simple arguments. First we start from Q_i and draw a straight line on the cylinder surface parallel to the cylinder axis. This line will intersect with the circle centered at O . We call the point B . Similarly we can find point A starting with point Q_o . Since $\overline{OA} = \overline{OB} = r$, the radius of the cylinder, $\triangle OAB$ is isosceles. By symmetry,

$\triangle OQA$ is congruent to $\triangle OQB$, and therefore \overline{OQ} is perpendicular to \overline{AB} . Meanwhile, $\triangle QBQ_i$ and $\triangle QAQ_o$ are also right triangles. From $\triangle OQB$ and $\triangle QBQ_i$ we have the relation

$$\overline{QB}^2 = \ell^2 \sin^2 \theta = \overline{OB}^2 - \overline{OQ}^2 \quad (\text{A.9})$$

$$\Rightarrow \ell = \frac{\sqrt{r^2 - d^2}}{\sin \theta} \quad (\text{A.10})$$

Once ℓ is known, Q_i and Q_o are also known.

The last step is to restore the top and bottom planes of the cylinder and rescale the solution points if necessary. In order to simply the notation, here we adopt the coordinate system with the origin at the cylinder center and the z axis parallel to the cylinder axis. In this coordinate system the top cylinder plane has the equation $z = z_t$ and bottom plane has the equation $z = z_b$. Suppose in this coordinate system Q_i has coordinate $Q_i(q_{ix}, q_{iy}, q_{iz})$. There are three conditions concerning to the ordering of q_{iz} , z_t and z_b :

1. $q_{iz} < z_b$. There is no solution to this problem.
2. $z_b < q_{iz} < z_t$. Q_i is the right answer and nothing has to be done.
3. $z_t < q_{iz}$. Q_i has to be moved along the track line until it touches the top plane. The new point is

$$\vec{q}'_i = \vec{q} - \frac{z_t - q_z}{q_{iz} - q_z} \hat{v} \quad (\text{A.11})$$

where Q has the coordinate $Q(q_x, q_y, q_z)$ and \hat{v} has a direction with $v_z < 0$.

We do ~~a~~ similar check on the point Q_o . If there is ~~a~~ solution, the track length is $\overline{Q_i Q_o}$. ↗

Now we look at the problem of finding a cylindrical fiducial volume with an arbitrary axis inside a bigger cylinder so that it has the maximum length and is completely inscribed in the bigger cylinder.

$\hat{v} = (v_x, v_y, v_z)$, by substituting the coordinates and numbers into Equation A.12 we obtain

$$(1 - v_z^2)Z - 2v_z(v_x X + v_y Y)Z + [X^2 + Y^2 - (v_x X + v_y Y)^2 - r^2] = 0 \quad (\text{A.13})$$

where

$$X = R \cos \phi - p_{0x} \quad (\text{A.14})$$

$$Y = R \sin \phi - p_{0y} \quad (\text{A.15})$$

$$Z = z - p_{0z} \quad (\text{A.16})$$

For each value of ϕ there is a corresponding quadratic equation. Practically we can scan for ϕ with some small step, solve the equation for z and find the coordinates of the points in the common curve. Usually there are ϕ values with two real roots and ϕ values without any real root. This is due to the topology of the intersection curve. We plot the z versus ϕ plot. If there is solution to this problem, there are two closed curves in this plot. If there are less than two curves, there is no solution. Figure A.3 and Figure A.4 show examples without and with solution. From the figures we clearly see that the problem has solution only if there are two closed curves. Here we also introduce a convenient track coordinate, with origin at the point of the track line p_0 and a t axis along the track's direction vector \hat{v} . For each point in each closed curve we can calculate the t -value by projection,

$$t = (\vec{p} - \vec{p}_0) \cdot \hat{v} \quad (\text{A.17})$$

Now we look for the four numbers,

$$t_M^{(i)} = \sup \left\{ t^{(i)} | \vec{p}^{(i)} \in C^{(i)} \right\} \quad (\text{A.18})$$

$$t_m^{(i)} = \inf \left\{ t^{(i)} | \vec{p}^{(i)} \in C^{(i)} \right\} \quad (\text{A.19})$$

Bibliography

- [1] C. L. Cowan Jr., F. Reines, F. B. Harrison, H. W. Kruse, A. D. McGuire, "Detection of the Free Neutrino: a Confirmation," *Science* **124** (3212): 103–4, 1956.
- [2] B. Pontecorvo, Sov. Phys. JETP **6**, 429, 1957.
- [3] W. C. Carithers et al., "Measurement of the Phase of the CP-Nonconservation Parameter η_{+-} and the K_S Total Decay Rate," *Phys. Rev. Lett.* **34**, 1244, 1975.
- [4] A. Das and T. Ferbel, *Introduction to Nuclear and Particle Physics*. World Scientific Publishing Co. Pte. Ltd., 2003.
- [5] J. Bahcall, "Solar Models: An Historical Overview," *Nuclear Physics B (Proc. Suppl.)* **118** (2003) 77–86, 2003.
- [6] G. Danby, J-M. Gaillard, K. Goulian, L. M. Lederman, N. Mistry, M. Schwartz, and J. Steinberger, "Observation of High-Energy Neutrino Reactions and the Existence of Two Kinds of Neutrinos," *Phys. Rev. Lett.* **9**, 36, 1962. *see [9] - Be consistent*
- [7] V. Gribov, B. Pontecorvo, *Physics Letters B* **28** (7): 493–496, 1969.
- [8] DONUT Collaboration, "Observation of tau neutrino interactions," *Phys. Lett. B* **504** (3): 218, 2001. *Be consistent*

see [6] Be consistent

- [9] Y. Fukuda et al., "Evidence for oscillation of atmospheric neutrinos," *Physical Review Letters* **81** (8): 1562–1567, 1998.

- [10] K.A. Olive et al. (Particle Data Group), "The Review of Particle Physics," *Chin. Phys. C* **38**, 090001, 2014.

- [11] J. W. F. Valle, "Neutrino physics overview," *Journal of Physics: Conference Series* **53**: 473, 2006.

- [12] Daya Bay Collaboration, *Daya Bay Project Technical Design Report (v2)*. Daya Bay Collaboration, 2008.

- [13] V. I. Kopeikin, L. A. Mikaelyan, and V. V. Sinev, "Reactor as a Source of Antineutrinos: Thermal Fission Energy," *Physics of Atomic Nuclei*, vol. 67, pp. 1892–1899, 2004.

- [14] P. Vogel and J. Engel, "Neutrino electromagnetic form factors," *Physical Review D*, vol. 39, p. 3378, 1989.

- [15] P. Vogel and J. F. Beacom, "Angular distribution of neutron inverse beta decay, $\bar{\nu}_e + p \rightarrow e^+ + n$," *Physical Review D*, vol. 60 053003, 1999.

- [16] Liang Zhan, "Determine Theta13 Using Chisquare fit (Tech Note)." DocDB-7610.

- [17] F. P. An et al. (Daya Bay Collaboration), "Improved Measurement of Electron Antineutrino Disappearance at Daya Bay." Chinese Phys. C **37** 011001, 2013.

- [18] L.A. Mikaelyan and V.V. Sinev. *Phys. Atom. Nucl.* **63**, 1002, 2000.

- [19] J. Beringer et al.(PDG), "COSMIC RAYS," *PR D86*, 010001, 2012. p#?

- [20] F. P. An et al. (Daya Bay Collaboration), "Observation of Electron-Antineutrino Disappearance at Daya Bay." *Phys. Rev. Lett.* **108**, 171803, 2012. p#?

[21] Hamamatsu, "Large Photocathode Area Photomultiplier Tubes." R5912-02 Datasheet.

[22] W. Beriguete et al., "Production of Gadolinium-loaded Liquid Scintillator for the Daya Bay Reactor Neutrino Experiment," *arXiv:1402.6694*, 2014.

[23] DuPont™. DuPont™Tyvek®. *expand*

[24] F. P. An et al. (Daya Bay Collaboration), "A side-by-side comparison of Daya Bay antineutrino detectors." *Nucl. Instr. and Meth. A 685*, 78, 2012.

[25] F. P. An et al. (Daya Bay Collaboration), "The Muon System of the Daya Bay Reactor Antineutrino Experiment." *arXiv:1407.0275*, 2014.

[26] Ji-Lei Xu et al., "Design and preliminary test results of Daya Bay RPC modules," *Chinese Phys. C 35* 844, 2011.

[27] Z. Ning et al., "Calibration algorithms of RPC detectors at Daya Bay Neutrino Experiment," *JINST 8 T03007*, 2013.

[28] "VMEbus Specification Manual." <https://www.mpp.mpg.de/~huber/vme/vmebus.pdf>, 1985.

[29] H. Gong et al., "Design of the Local Trigger Board for the Daya Bay Reactor Neutrino Experiment," *Nucl. Inst. and Meth. A 637* (2011) 138, 2011.

[30] Ying-Biao Liu et al., "Onsite data processing and monitoring for the Daya Bay Experiment." *arXiv:1406.2104*, 2013.

[31] Simon Patton, "SPADE - An Introduction." DocDB-2696.

[32] "Daya Bay Offline User Manual." <http://dayabay.bnl.gov/oum/>.

[33] "The Gaudi Project." <http://proj-gaudi.web.cern.ch/proj-gaudi/>.

- Font*
- [34] R. Santonico and R. Cardarelli, "Development of Resistive Plate Counters," *Nuclear Instruments and Methods*, vol. 187, pp. 377–380, 1981.
- [35] Ji-Feng Han et al., "Test of BESIII RPC in the avalanche mode," *Chinese Phys. C* 32 373, 2008.
- [36] Qingmin Zhang et al., "An underground cosmic-ray detector made of RPC," *Nucl. Instrum. Meth. A* 583 (2007) 278-284, 2007.
- [37] Lie-Hua Ma et al., "A Study of RPC Gas Composition using Daya Bay RPCs," *Chinese Phys. C* 34 (2010) 1116-1121, 2010.
- [38] Lie-Hua Ma et al., "The mass production and quality control of RPCs for the Daya Bay Experiment," *Nucl. Instrum. Meth. A* 659 (2011) 154-160, 2011.
- [39] Jiawen Zhang et al., "The design and mass production on Resistive Plate Chambers for the BESIII experiment," *Nucl. Instrum. Meth. A* 580 (2007) 1250–1256, 2007.
- [40] Werner Riegler, Daniel Burgarth, "Signal propagation, termination, crosstalk and losses in resistive plate chambers," *Nucl. Instrum. Meth. A* 481 (2002) 130–143, 2002.
- [41] Cheng-ju Lin, Yasuhiro Nakajima, J. Pedro Ochoa and Patrick Tsang, "The adsimple reconstruction." DocDB-7334. *where*
- [42] L. Wang, "Muon track reconstruction." DocDB-7838. *where*
- [43] Yue Meng, "WP PMT & timing Calibration." DocDB-7696. *where*
- [44] Joseph A. Formaggio and C.J. Martoff, "BACKGROUND TO SENSITIVE EXPERIMENTS UNDERGROUND," *Annu. Rev. Nucl. Part. Sci.* 2004. 54:361–412, 2004.
- [45] Thomas Luu and Christian Hagmann, "Neutron Production by Muon Spallation I: Theory," UCRL-TR-226323, 2006.
- Font*

- [46] Jean Delorme and Magda Ericson, "Pion and neutron production by cosmic-ray muons underground," *Phys. Rev. C* **52**, 2222, 1995.
- [47] M.V. Kossov, "Approximation of photonuclear interaction cross-sections," *The European Physical Journal A - Hadrons and Nuclei* July 2002, Volume 14, Issue 3, pp 377-392, 2002. *format*
- [48] P. F. Bortignon, A. Bracco, and R. A. Broglia, *Giant Resonances : Nuclear Structure at Finite Temperature*. CRC Press, 1998.
- [49] IAEA Photonuclear Data Library. *titles* *format*
- [50] J. Ling and H. Lu, "Muon tagging." DocDB-6759. *titles* *format*
- [51] G. T. Zatsepin and O. G. Ryazhskaya, *Izv. Akad. Nauk SSSR, Ser. Fiz.* **29**, 1946, 1965. *titles*
- [52] Y.-F. Wang et al., *Phys. Rev. D* **64**, 013012, 2001. *titles*
- [53] H. M. Araujo et al., *Nucl. Instrum. Methods A* **545**, 398, 2005. *titles*
- [54] D.-M. Mei and A. Hime, *Phys. Rev. D* **73**, 053004, 2006. *titles*
- [55] A. S. Malgin and O. G. Ryazhskaya, "Neutrons from Muons Underground," *Physics of Atomic Nuclei*, vol. 71, pp. 1769-1781, 2008. *format* *titles*
- [56] G. V. Gorshkov, V. A. Zyabkin, and R. M. Yakovlev, *Sov. J. Nucl. Phys.* **13**, 450, 1971. *titles*
- [57] L. B. Bezrukov et al., *Sov. J. Nucl. Phys.* **17**, 51, 1973. *titles*
- [58] L. B. Bezrukov et al., *Sov. J. Nucl. Phys.* **46**, 1492, 1987. *format*
- [59] M. Aglietta et al., *Nuovo Cimento C* **12**, 467, 1989.
- [60] Minfang Yeh, "Property of Daya Bay ADs 1-6 Liquids (Gd-LS, LS and MO)." DocDB-6615. *titles*

- open
re source*
- [61] G. Li and J. Liu, "Absolute h-gd ratio study with spallation and amc neutrons." DocDB-7273.
 - [62] B. Littlejohn, "Absolute neutron capture ratios." DocDB-7524.
 - [63] F. Wu and X. Qian, "H-gd ratio with spallation neutron and amc source." DocDB-7525.
 - [64] J. Ling and X. Qian, "Puc special acu long run study." DocDB-8280.
 - [65] M. Yang, "Neutron capture ratio on gd." DocDB-8473.
 - [66] G. L. J. Liu, "H/gd ratio from special acu runs." DocDB-8501.
 - [67] Z. Yu, "Summary and perspective of gd capture ratio." DocDB-9226.
 - [68] G. Li, "Constrain center gd capture ratio with special acu data." DocDB-9273.
 - [69] Guofu Cao, "A Cross Check for H/Gd Ratio." DocDB-7730.
 - [70] Xin Qian and Chao Zhang, "Understanding the Gd Neutron Capture Timing Spectrum." DocDB-7299.
 - [71] (Daya Bay Collaboration), "Daya Bay Proposal." arXiv:hep-ex/0701029, 2007.
 - [72] A Empl, E. V. Hungerford, R. Jasim, P. Mosteiro, "A Fluka Study of Underground Cosmogenic Neutron Production," arXiv:1406.6081, 2014.
 - [73] N. Yu. Agafonova, A. S. Malgin. arXiv:1304.0919, 2013.
- title*